

# Theoretical modeling and experimental demonstration of Raman probe induced spectral dip for realizing a superluminal laser

JOSHUA YABLON,<sup>1,\*</sup> ZIFAN ZHOU,<sup>1</sup> MINCHUAN ZHOU,<sup>2</sup> YE WANG,<sup>1</sup> S. TSENG,<sup>3</sup> AND M. S. SHAHRIAR<sup>1,2</sup>

<sup>1</sup>Northwestern University, Department of Electrical Engineering and Computer Science, Evanston, IL 60208, USA

<sup>2</sup>Northwestern University, Department of Physics and Astronomy, Evanston, IL 60208, USA

<sup>3</sup>Digital Optics Technologies, Rolling Meadows IL, 60008 USA

\*[joshuayablon2014@u.northwestern.edu](mailto:joshuayablon2014@u.northwestern.edu)

**Abstract:** We have demonstrated experimentally a Diode-Pumped Alkali Laser (DPAL) with a Raman resonance induced dip in the center of the gain profile, in order to produce an anomalous dispersion, necessary for making the laser superluminal. Numerical calculations match closely with experimental results, and indicate that the laser is operating superluminally, with the group index far below unity ( $\sim 0.00526$ ) at the center of the dip. The estimated factor of enhancement in the sensitivity to cavity length perturbation is  $\sim 190$ , approximately equaling the inverse of the group index. This enhancement factor can be made much higher via optimal tuning of parameters. Such a laser has the potential to advance significantly the field of high-precision metrology, with applications such as vibrometry, accelerometry, and rotation sensing.

© 2016 Optical Society of America

**OCIS codes:** (020.1670) Coherent optical effects; (120.3180) Interferometry; (140.3370) Laser gyroscopes; (190.5650) Raman effect.

## References and links

1. M. S. Shahriar, G. S. Pati, R. Tripathi, V. Gopal, M. Messall, and K. Salit, "Ultrahigh enhancement in absolute and relative rotation sensing using fast and slow light," *Phys. Rev. A* **75**(5), 053807 (2007).
2. D. D. Smith, H. Chang, L. Arissian, and J. C. Diels, "Dispersion-enhanced laser gyroscope," *Phys. Rev. A* **78**(5), 053824 (2008).
3. G. S. Pati, M. Salit, K. Salit, and M. S. Shahriar, "Demonstration of displacement-measurement-sensitivity proportional to inverse group index of intra-cavity medium in a ring resonator," *Opt. Commun.* **281**(19), 4931–4935 (2008).
4. D. D. Smith, K. Myneni, J. A. Odutola, and J. C. Diels, "Enhanced sensitivity of a passive optical cavity by an intracavity dispersive medium," *Phys. Rev. A* **80**(1), 011809 (2009).
5. D. D. Smith, H. Chang, K. Myneni, and A. T. Rosenberger, "Fast-light enhancement of an optical cavity by polarization mode coupling," *Phys. Rev. A* **89**(5), 053804 (2014).
6. G. S. Pati, M. Salit, K. Salit, and M. S. Shahriar, "Demonstration of a tunable-bandwidth white-light interferometer using anomalous dispersion in atomic vapor," *Phys. Rev. Lett.* **99**(13), 133601 (2007).
7. O. Kotlicki, J. Scheuer, and M. S. Shahriar, "Theoretical study on Brillouin fiber laser sensor based on white light cavity," *Opt. Express* **20**(27), 28234–28248 (2012).
8. K. Myneni, D. D. Smith, H. Chang, and H. A. Luckay, "Temperature sensitivity of the cavity scale factor enhancement for a Gaussian absorption resonance," *Phys. Rev. A* **92**(5), 053845 (2015).
9. H. N. Yum, M. Salit, J. Yablon, K. Salit, Y. Wang, and M. S. Shahriar, "Superluminal ring laser for hypersensitive sensing," *Opt. Express* **18**(17), 17658–17665 (2010).
10. G. S. Pati, M. Salit, K. Salit, and M. S. Shahriar, "Simultaneous slow and fast light effects using probe gain and pump depletion via Raman gain in atomic vapor," *Opt. Express* **17**(11), 8775–8780 (2009).
11. J. Scheuer and S. M. Shahriar, "Lasing dynamics of super and sub luminal lasers," *Opt. Express* **23**(25), 32350–32366 (2015).
12. W. F. Krupke, R. J. Beach, V. K. Kanz, and S. A. Payne, "Resonance transition 795-nm rubidium laser," *Opt. Lett.* **28**(23), 2336–2338 (2003).
13. M. O. Scully, and W. E. Lamb, *Laser Physics* (Westview, 1974).
14. H. C. Bolton and G. J. Troup, "The modification of the Kronig-Kramers relations under saturation conditions," *Philos. Mag.* **19**(159), 477–485 (1969).

15. G. J. Troup and A. Bambini, "The use of the modified Kramers-Kronig relation in the rate equation approach of laser theory," *Phys. Lett.* **45**(5), 393–394 (1973).
16. H. N. Yum and M. S. Shahriar, "Pump-probe model for the Kramers-Kronig relations in a laser," *J. Opt.* **12**(10), 104018 (2010).
17. T. Skettrup, T. Meelby, K. Faerch, S. L. Frederiksen, and C. Pedersen, "Triangular laser resonators with astigmatic compensation," *Appl. Opt.* **39**(24), 4306–4312 (2000).
18. Z. Zhou, J. Yablon, M. Zhou, Y. Wang, A. Heifetz, and M. S. Shahriar, "Modeling and analysis of an ultra-stable subluminal laser," *Opt. Commun.* **358**, 6–19 (2016).
19. M. S. Shahriar, Y. Wang, S. Krishnamurthy, Y. Tu, G. S. Pati, and S. Tseng, "Evolution of an N-level system via automated vectorization of the Liouville equations and application to optically controlled polarization rotation," *J. Mod. Opt.* **61**(4), 351–367 (2014).
20. D. A. Steck, "Rubidium 85 D Line Data," available online at <http://steck.us/alkalidata> (revision 2.1.6, 20 September 2013).
21. D. A. Steck, "Rubidium 87 D Line Data," available online at <http://steck.us/alkalidata> (revision 2.0.1, 2 May 2008).
22. Y. Wang, Z. Zhou, J. Yablon, and M. S. Shahriar, "Effect of multi-order harmonics in a double-Raman pumped gain medium for a superluminal laser," *Opt. Eng.* **54**(5), 057106 (2015).

## 1. Introduction

Optical interferometry is currently the standard technique for making many of the most precise measurements, but there still exist many applications for which even the best interferometers are not sensitive enough, and some applications for which higher sensitivity will always be of interest. Over the last few years, significant effort has been underway towards theoretical understanding and experimental realization of superluminal lasers, with the ultimate goal of metrological sensitivity enhancement [1–11]. It has been shown that the sensitivity of a ring laser with respect to cavity length perturbation is inversely proportional to the group index of the material inside the cavity [3,8]. By definition, the group velocity of a superluminal laser exceeds the velocity of light in vacuum, which means that the group index,  $n_g$ , is less than unity. In principle any value of  $n_g$  can be achieved with the proper choice of experimental parameters; therefore creating a laser with group index arbitrarily close to zero over a significant bandwidth is the ultimate goal of superluminally-enhanced laser interferometry.

Previously we described a general scheme for realizing a superluminal laser in which the laser gain profile contains a narrow absorption dip at the center [9]. Within the range of this dip, the lasing beam itself experiences anomalous dispersion. Figure 1(a) shows a typical gain profile ( $-\chi''$ ) within this range, while the corresponding variation in the index ( $\chi'$ ) is shown in Fig. 1(b). The slope of the index at the center of the dip is negative, which corresponds to anomalous dispersion and therefore superluminal operation. With properly-tuned parameters,  $n_g^{-1}$  can exceed  $10^5$  over a significant bandwidth, leading to sensitivity enhancement of more than five orders of magnitude. This is calculated and described in detail in [9].

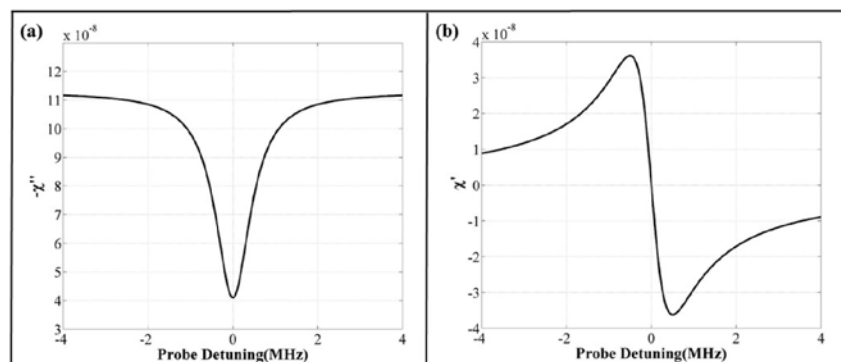


Fig. 1. (a) Spectral profile of the gain ( $-\chi''$ ) vs. probe frequency in the vicinity of the dip; (b) Index ( $\chi'$ ) in the vicinity of the dip

We have demonstrated this scheme by using Raman depletion inside a Diode-Pumped Alkali Laser (DPAL) cavity, as shown in Fig. 2. The process starts by creating a ring laser for which gain is provided by an optically-pumped Rubidium vapor cell containing a high-pressure buffer gas [12]. A Raman probe is then created by taking a piece of the output beam and frequency-shifting it by an amount that matches the ground-state hyperfine splitting in  $^{85}\text{Rb}$ . Another vapor cell (without buffer gas) is placed inside the cavity and is optically pumped so that population imbalance between the two hyperfine ground states is achieved. This leads to gain in the Raman probe, accompanied by depletion of the intra-cavity beam, which effectively serves as the Raman pump in this process.

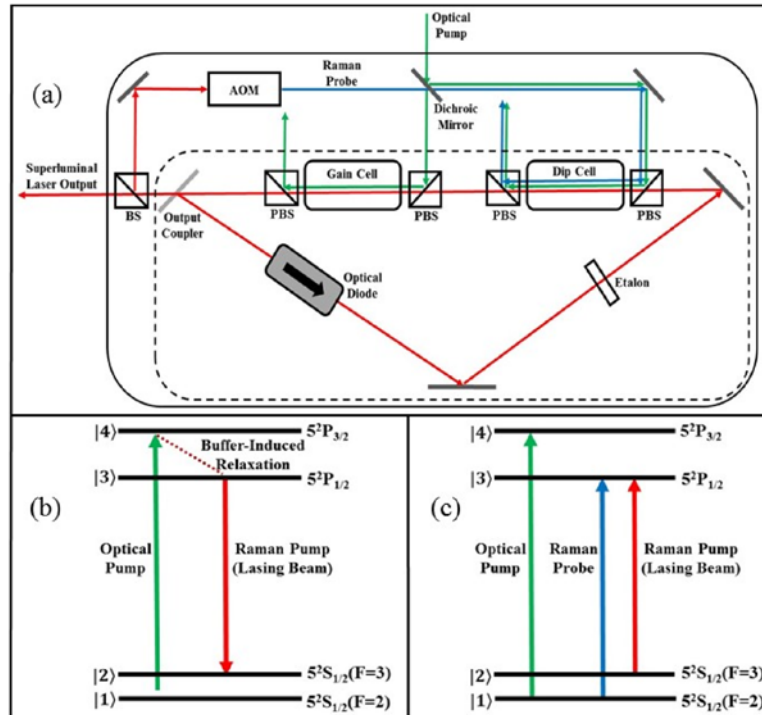


Fig. 2. (a) Schematic of superluminal laser; (b) Energy levels and optical fields in the gain cell; (c) Energy levels and optical fields in the dip cell

The goal of this paper is to present our experimental work regarding the realization of such a scheme, and to compare our findings with the numerical model which we have developed. In the next section, we review briefly the analytical description of the superluminal lasing process, which makes use of idealized gain and dip profiles. We then present our design of the superluminal laser, and describe a more comprehensive numerical model based on the density matrices of the atomic systems that provide the DPAL gain and Raman depletion. Finally, we show the experimental results and compare them to predictions made by the numerical model. The correspondence between theory and experiment suggests that our laser is operating in the superluminal regime.

## 2. Analytical model of a laser with idealized Lorentzian gain and dip

To understand and quantify the enhancement effects in a superluminal laser, it is important to review briefly the semi-classical equations of motion for a single-mode laser [13]. The phase and amplitude of the electric field in an optical cavity are governed by the following equations:

$$\nu + \dot{\varphi} = \Omega_c - \frac{\chi_R}{2} \nu \quad (1)$$

$$\dot{E} = -\frac{\nu E}{2Q} - \frac{\chi_I E}{2} \nu \quad (2)$$

where  $\nu$  is the frequency, and  $\varphi$  and  $E$  are the phase and amplitude of the lasing field.  $\Omega_c$  is the empty-cavity resonant frequency for a particular longitudinal mode, and  $Q$  is the quality factor of the empty cavity. The material susceptibility is  $\chi = \chi_R + i\chi_I$  where  $\chi_R$  and  $\chi_I$  characterize the material dispersion and gain/loss, respectively.

The derivatives  $d\nu/dL$  and  $d\Omega_c/dL$  characterize the sensitivity of the laser output frequency with respect to cavity length change in a filled cavity and an empty cavity, respectively. The ratio between these two derivatives,  $R \equiv (d\nu/dL)/(d\Omega_c/dL)$  is therefore the factor by which the presence of the intra-cavity medium enhances ( $R > 1$ ) or reduces ( $R < 1$ ) frequency shift sensitivity. Solving Eqs. (1) and (2) in the steady state results in:

$$R = 1 / \left( 1 + \frac{\chi_R}{2} + \frac{\nu}{2} \frac{d\chi_R}{d\nu} \right) \quad (3)$$

To relate this enhancement factor to the group index, we start with:

$$n = (1 + \chi_R)^{1/2} = 1 + \frac{\chi_R}{2} - \frac{\chi_R^2}{4} + \frac{3\chi_R^3}{8} - \dots \quad (4)$$

In a dilute gas such as Rubidium vapor, the magnitude of  $\chi_R$  is far less than unity, so that only the first two terms of Eq. (4) are relevant. The group index  $n_g$  is the ratio between the vacuum speed of light  $c$  and group velocity, and can be expressed as follows:

$$n_g \equiv \frac{c}{v_g} = \frac{c}{\partial\omega/\partial k} = \frac{\partial(n\nu)}{\partial\nu} = \frac{\partial}{\partial\nu} \left[ \nu \left( 1 + \frac{\chi_R}{2} \right) \right] = 1 + \frac{\chi_R}{2} + \frac{\nu}{2} \frac{d\chi_R}{d\nu} \quad (5)$$

Therefore the enhancement factor  $R$  from Eq. (3) is the reciprocal of the group index. To obtain an analytic expression for  $R$ , we must first obtain an analytic expression for  $\chi_R(\nu)$ . We consider a Lorentzian gain medium with a Lorentzian inner dip, both centered at  $\nu = \nu_o$ , so that the imaginary part of the susceptibility  $\chi_I(\nu)$ , which represents gain (negative values) or loss (positive values), can be written as:

$$\chi_I(\nu) = -\frac{G_g \Gamma_g^2}{2\Omega_g^2 + \Gamma_g^2 + 4(\nu - \nu_o)^2} + \frac{G_d \Gamma_d^2}{2\Omega_d^2 + \Gamma_d^2 + 4(\nu - \nu_o)^2} \quad (6)$$

where the subscripts  $g$  and  $d$  refer to “gain” and “dip” respectively.  $\Omega_{g/d}$  is the transition Rabi frequency,  $\Gamma_{g/d}$  is the transition linewidth, and  $G_{g/d}$  is the strength parameter which depends on the number density of atoms as well as atomic dipole moment and transition linewidth. Applying the Modified Kramers-Kronig (MKK) relations [14–16] to Eq. (6) results in the following expression for the dispersion:

$$\chi_R(\nu) = \frac{2G_g (\nu - \nu_o) \Gamma_g}{2\Omega_g^2 + \Gamma_g^2 + 4(\nu - \nu_o)^2} - \frac{2G_d (\nu - \nu_o) \Gamma_d}{2\Omega_d^2 + \Gamma_d^2 + 4(\nu - \nu_o)^2} \quad (7)$$

With an analytic expression for  $\chi_R(\nu)$ , an analytic expression for  $R$  is obtainable using Eq. (3).

### 3. Superluminal laser design

The overall design for the superluminal laser is illustrated schematically in Fig. 2(a). The diagram of the energy levels and optical fields in the gain cell is shown in Fig. 2(b). The gain cell contains vapor of naturally-occurring Rubidium (72.16%  $^{85}\text{Rb}$  and 27.84%  $^{87}\text{Rb}$ ) mixed with high-pressure Ethane buffer gas, which induces rapid collisional relaxation from the  $P_{3/2}$  to the  $P_{1/2}$  manifold. This leads to population inversion and gain on the  $D_1$  line. The magnitude and bandwidth of the gain depend on the rate of collisions between the Rubidium atoms and the buffer gas molecules, so that the gain spectrum can be tuned to some extent by varying the buffer gas pressure.

The dip cell contains pure  $^{85}\text{Rb}$  vapor with no buffer gas. The two ground-state hyperfine levels are denoted as  $|1\rangle$  and  $|2\rangle$ ; however it is important to note that these states themselves are composed of five and seven Zeeman sublevels, respectively. The energy difference between these composite states  $|1\rangle$  and  $|2\rangle$  [Fig. 2(c)] is far less than the thermal energy at room temperature, so that if each Zeeman sublevel is equally-populated, then the composite states  $|1\rangle$  and  $|2\rangle$  contain 5/12 and 7/12 of the total atomic population, respectively. In order to produce Raman gain and depletion, it is necessary to produce first a population imbalance between two different Zeeman sublevels. This is the purpose of the Raman optical pump [Fig. 2(c)], which transfers atoms from the Zeeman sublevels in state  $|1\rangle$  to the Zeeman sublevels in state  $|2\rangle$ .

The Raman probe is produced by frequency-shifting the laser output with an acousto-optic modulator (AOM) by approximately 3.0357 GHz, which is the ground-state hyperfine splitting in  $^{85}\text{Rb}$ . Two-photon resonance between the Raman probe and the lasing beam results in amplification of the Raman probe, at the expense of the lasing beam which thus experiences depletion. In general, this Raman gain/depletion process is most efficient when the Raman pump and probe are slightly detuned from resonance, so that single-photon absorption is minimized.

The cavity contains a flat output coupler and two curved high reflectors. Cavity length and reflector radii of curvature are specifically chosen so that a stable and astigmatism-free mode exists without the use of an intra-cavity lens [17]. To avoid Zeeman splitting, the dip cell is placed inside a mu-metal box. The optical isolator prevents directional mode competition, while the etalon prevents longitudinal mode competition and enables manual tunability of optical path length. Transverse mode competition can be eliminated with the proper choice of optical pump beam radius, or with the insertion of an intra-cavity aperture.

### 4. Numerical model of a superluminal laser

In order to calculate and analyze accurately the dynamics of the DPAL-Raman system described in section 3, it is necessary to use numerical methods. Though the analytic model from section 2 is instructive, it relies on the assumption that the gain and dip profiles are Lorentzians with fixed parameters. While this is a good first-order approximation, the exact characteristics of the gain and dip profiles depend on many interconnected variables. Our numerical approach relies on solving the single mode laser equations [Eqs. (1) and (2)] and the density-matrix equations simultaneously and iteratively until a self-consistent, steady-state solution is found. The algorithmic procedure is illustrated in Fig. 3; a more detailed discussion of this algorithm can be found in [18].

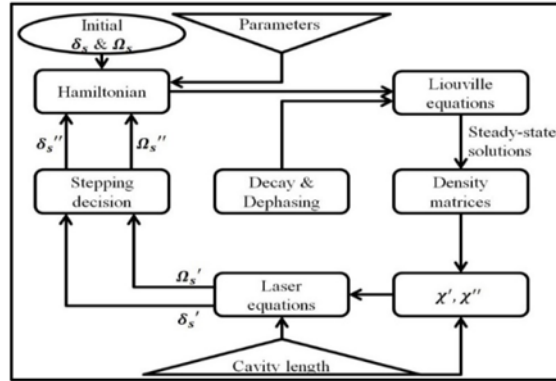


Fig. 3. Flow chart illustrating the iterative algorithm used to calculate laser output frequency and amplitude.

#### 4.1 Calculation of the density matrix of the gain system

The gain cell contains vapor of naturally-occurring Rubidium mixed with Ethane buffer gas. Both isotopes are modeled as four-level systems. Figure 4 illustrates this system for the  $^{85}\text{Rb}$  isotope. Here  $|1\rangle$  and  $|2\rangle$  are the  $F = 2$  and  $F = 3$  hyperfine states, respectively, in the  $5S_{1/2}$  manifold.  $|3\rangle$  is the entire  $5P_{1/2}$  manifold, and  $|4\rangle$  is the entire  $5P_{3/2}$  manifold. For  $^{87}\text{Rb}$ ,  $|1\rangle$  and  $|2\rangle$  are the  $F = 1$  and  $F = 2$  hyperfine states, respectively, in the  $5S_{1/2}$  manifold.  $|3\rangle$  is the  $5P_{1/2}$  manifold, and  $|4\rangle$  is the  $5P_{3/2}$  manifold. The buffer gas causes rapid dephasing in both isotopes, thus producing homogeneous broadening of several tens of GHz, depending on the buffer gas pressure. Therefore it is unnecessary to consider the hyperfine sublevels within the  $5P_{1/2}$  and  $5P_{3/2}$  manifolds. The BGI (buffer gas-induced) broadening is also wider than the splitting between  $|1\rangle$  and  $|2\rangle$ , so that the optical pump excites atoms from both  $|1\rangle$  and  $|2\rangle$  into  $|4\rangle$ . The strengths of the  $|1\rangle$ - $|4\rangle$  and  $|2\rangle$ - $|4\rangle$  transitions (i.e. their Rabi frequencies) are assumed to be equal for simplicity, and denoted as  $\Omega_p$ . The  $|1\rangle$ - $|3\rangle$  and  $|2\rangle$ - $|3\rangle$  transitions, which are coupled by the intra-cavity lasing beam itself, are also assumed to be equal in strength, and are labeled as  $\Omega_L$ .  $\Gamma_{3R}$  and  $\Gamma_{4R}$  are the inverse radiative lifetimes of the  $5P_{1/2}$  and  $5P_{3/2}$  manifolds, and are equal to  $36.1 \times 10^6 \text{ sec}^{-1}$  and  $38.1 \times 10^6 \text{ sec}^{-1}$ , respectively. The decay rates  $\Gamma_{31}$  and  $\Gamma_{32}$  are assumed to be equal so that  $\Gamma_{31} = \Gamma_{32} = \Gamma_{3R} / 2$ ; the same is true for  $\Gamma_{41}$  and  $\Gamma_{42}$ . At experimental temperatures (approximately  $120^\circ\text{C}$ ), the hyperfine splitting values  $\Delta E_{12}$  and  $\Delta E_{34}$  are several orders of magnitude smaller than  $k_B T$ , so that the ratios  $\Gamma_{12} / \Gamma_{21}$  and  $\Gamma_{34} / \Gamma_{43}$  are determined only by the ratios of the Zeeman degeneracies, and are equal to  $7/5$  and  $2$ , respectively for  $^{85}\text{Rb}$ .

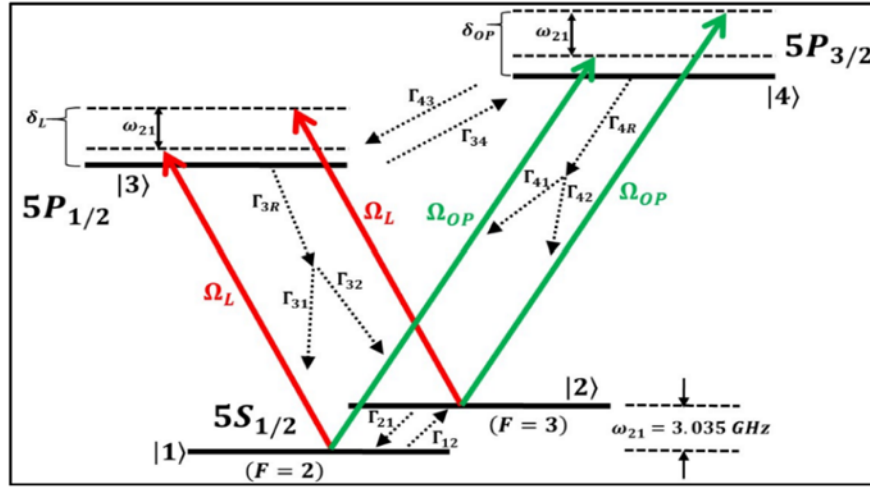


Fig. 4. Illustration of the energy levels, optical fields and decay rates for the gain cell.

The Liouville equation [18,19] is the density matrix equation of evolution:

$$\frac{\partial}{\partial t} \tilde{\rho}_G = -\frac{i}{\hbar} [\tilde{H}_G, \tilde{\rho}_G] + \frac{\partial \tilde{\rho}_G}{\partial t}_{SOURCE} + \frac{\partial \tilde{\rho}_G}{\partial t}_{DEPHASING} \quad (8)$$

where  $\tilde{\rho}_G$  and  $\tilde{H}_G$  are the density matrix and the modified Hamiltonian, respectively, of the gain medium in the rotating wave basis. In Eq. (8), the second term accounts for equality between net population inflows and outflows, and the third term accounts for the BGI dephasing between different states.

The modified rotating-wave Hamiltonian of this gain system is expressed as:

$$\begin{aligned} \tilde{H}_G = & \frac{\hbar}{2} [(-i\Gamma_{12}) |1\rangle\langle 1| + (2\omega_{21} - i\Gamma_{21}) |2\rangle\langle 2| + [-2\delta_L - i(\Gamma_{31} + \Gamma_{32} + \Gamma_{34})] |3\rangle\langle 3| \\ & + [-2\delta_{OP} - i(\Gamma_{41} + \Gamma_{42} + \Gamma_{43})] |4\rangle\langle 4| + \{\Omega_L |1\rangle\langle 3| + \Omega_{OP} |1\rangle\langle 4| \\ & + \Omega_L |2\rangle\langle 3| + \Omega_{OP} |2\rangle\langle 4| + h.c.\}] \end{aligned} \quad (9)$$

The source term in Eq. (8) is:

$$\begin{aligned} \frac{\partial \tilde{\rho}_G}{\partial t}_{SOURCE} = & (\Gamma_{21}\tilde{\rho}_{22} + \Gamma_{3R}\tilde{\rho}_{33}/2 + \Gamma_{4R}\tilde{\rho}_{44}/2) |1\rangle\langle 1| \\ & + (\Gamma_{12}\tilde{\rho}_{11} + \Gamma_{3R}\tilde{\rho}_{33}/2 + \Gamma_{4R}\tilde{\rho}_{44}/2) |2\rangle\langle 2| + \Gamma_{43}\tilde{\rho}_{44} |3\rangle\langle 3| + \Gamma_{34}\tilde{\rho}_{33} |4\rangle\langle 4| \end{aligned} \quad (10)$$

All six of the inter-level transitions are assumed to have equal BGI dephasing rates, denoted as  $\Gamma_d$ , so that the last term in Eq. (8) is:

$$\begin{aligned} \frac{\partial \tilde{\rho}_G}{\partial t}_{DEPHASING} = & -[\Gamma_d\tilde{\rho}_{12} |1\rangle\langle 2| + \Gamma_d\tilde{\rho}_{13} |1\rangle\langle 3| \\ & + \Gamma_d\tilde{\rho}_{14} |1\rangle\langle 4| + \Gamma_d\tilde{\rho}_{23} |2\rangle\langle 3| + \Gamma_d\tilde{\rho}_{24} |2\rangle\langle 4| + \Gamma_d\tilde{\rho}_{34} |3\rangle\langle 4| + h.c.] \end{aligned} \quad (11)$$

#### 4.2 Calculation of the density matrix of the dip system

The dip cell contains pure  $^{85}\text{Rb}$  vapor with no buffer gas, and has three different beams going through it, as shown in Fig. 5(a). Since the optical pump transfers population from level  $|1\rangle$  to  $|2\rangle$ , it can be modeled as an effective decay rate, denoted as  $\Gamma_{OP}$ . This enables the problem

to be analyzed as an effective 3-level system in which the decay rate from  $|1\rangle$  to  $|2\rangle$  is now  $\Gamma'_{12} \equiv \Gamma_{12} + \Gamma_{OP}$ , as illustrated in Fig. 5(b).

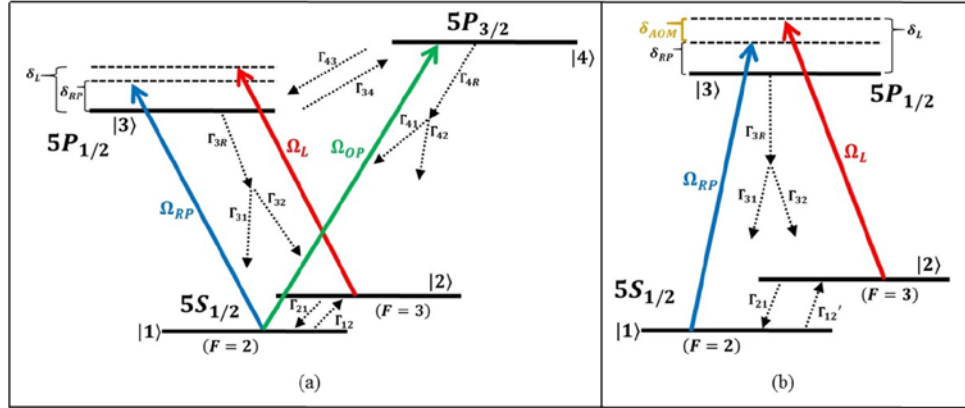


Fig. 5. (a) Illustration of the energy levels, optical fields and decay rates for the dip cell; (b) Effective 3-level system in which the optical pump is equivalently modeled as a decay rate

The density matrix equation of evolution for the dip system does not have a BGI dephasing term since the dip cell contains no buffer gas. Therefore:

$$\frac{\partial}{\partial t} \tilde{\rho}_D = -\frac{i}{\hbar} [\tilde{H}_D, \tilde{\rho}_D] + \frac{\partial \tilde{\rho}_D}{\partial t}_{SOURCE} \quad (12)$$

where:

$$\begin{aligned} \tilde{H}_D = \frac{\hbar}{2} \{ & (-i\Gamma_{12}) |1\rangle\langle 1| + (-2\delta_{RP} + 2\delta_L - i\Gamma_{21}) |2\rangle\langle 2| \\ & + (-2\delta_{RP} - i\Gamma_{3R}) |3\rangle\langle 3| + [\Omega_L |1\rangle\langle 3| + \Omega_{RP} |2\rangle\langle 3| + h.c.] \} \end{aligned} \quad (13)$$

and:

$$\frac{\partial \tilde{\rho}_D}{\partial t}_{SOURCE} = (\Gamma_{21}\tilde{\rho}_{22} + \Gamma_{3R}\tilde{\rho}_{33}/2) |1\rangle\langle 1| + (\Gamma_{12}\tilde{\rho}_{11} + \Gamma_{3R}\tilde{\rho}_{33}/2) |2\rangle\langle 2| \quad (14)$$

#### 4.3 Effective susceptibility of the superluminal laser

Due to BGI broadening in the gain cell, the lasing beam interacts with the  $|1\rangle$ - $|3\rangle$  and  $|2\rangle$ - $|3\rangle$  transitions in both the  $^{85}\text{Rb}$  and  $^{87}\text{Rb}$  isotopes. The susceptibility of this beam to  $^{85}\text{Rb}$  atoms in the gain cell,  $\chi_{G-85}$ , is related to the density matrix through the following relation [18]:

$$\chi_{G-85} = \left[ (\tilde{\rho}_{31}) \frac{\hbar c n_G}{I_{SAT(13)} \Omega_L} \left( \frac{\Gamma_{31}}{2} \right)^2 \right]_{85} + \left[ (\tilde{\rho}_{32}) \frac{\hbar c n_G}{I_{SAT(23)} \Omega_L} \left( \frac{\Gamma_{32}}{2} \right)^2 \right]_{85} \quad (15)$$

where  $n_G$  is the number density of gain atoms, and the “85” subscript refers to the  $^{85}\text{Rb}$  isotope.  $I_{SAT(13)}$  and  $I_{SAT(23)}$  are the effective saturation intensities of the  $|1\rangle$ - $|3\rangle$  and  $|2\rangle$ - $|3\rangle$  transitions, respectively. These quantities are calculated by averaging the saturation intensities of all constituent Zeeman transitions for  $\sigma^+$  or  $\sigma^-$  excitation (the actual polarization is linear, which consists of equal parts of  $\sigma^+$  and  $\sigma^-$ ).  $I_{SAT(13)}$  and  $I_{SAT(23)}$  are found to be 8.347 mW/cm<sup>2</sup>

and  $6.283 \text{ mW/cm}^2$ , respectively [20,21]. A similar expression applies for  $\chi_{G-87}$ , the susceptibility of  $^{87}\text{Rb}$  atoms, with  $I_{SAT(13)}$  and  $I_{SAT(23)}$  equaling  $7.011 \text{ mW/cm}^2$  and  $4.531 \text{ mW/cm}^2$ , respectively. The total susceptibility in the gain cell,  $\chi_G$ , is therefore:

$$\chi_G = 0.72\chi_{G-85} + 0.28\chi_{G-87} \quad (16)$$

where 72% and 28% are the natural abundance of these isotopes. There is no BGI broadening in the dip cell, so that the lasing beam only couples the  $|1\rangle - |3\rangle$  transition in the  $^{85}\text{Rb}$  isotope. Therefore the susceptibility in the dip cell is:

$$\chi_D = \left[ \frac{\hbar c n_D}{I_{SAT(13)} \Omega_L} \left( \frac{\Gamma_{3R}}{2} \right)^2 \tilde{\rho}_{31} \right]_{85} \quad (17)$$

Thus the effective susceptibility of the whole system is:

$$\chi_{EFF} = \frac{L_G}{L} \chi_G + \frac{L_D}{L} \chi_D \quad (18)$$

where  $L$  is cavity length, and  $L_G$  and  $L_D$  are the gain cell and dip cell lengths, respectively. The numerical model then solves the single-mode laser equations and determines the value of  $\chi_{eff}$  iteratively until a self-consistent steady-state solution is reached. Details regarding such an algorithm can be found in [18,19].

## 5 Experimental results and comparison with numerical model

Direct measurement of superluminal enhancement requires a high degree of classical noise suppression as well as fast servos to maintain a high degree of stability of the laser sources. In our experiment, these systems are not yet precise enough to perform direct measurements of enhancement. Effort is in progress to improve the stability of our apparatus to the level necessary for such a measurement. However, it is still possible to infer the degree of superluminal enhancement through a careful measurement and characterization of the dip observed in the laser output, and comparing the result with the theoretical model. Specifically, we first show that the theoretical results are in close agreement with the observed data for a range of sets of parameters. For each set of parameters, we then use the theoretical model to infer the corresponding group indices and superluminal enhancement factors.

### 5.1 Details of experimental setup

The experimental apparatus and setup are shown schematically in Fig. 6. The laser cavity is an equilateral triangle with each leg 24 cm in length. The output coupler is flat and has a reflectivity of 60% while the other two mirrors are high reflectors with 20 cm radii of curvature. As mentioned previously, these cavity dimensions and radii of curvature are chosen so that the laser output is astigmatism-free without the use of an intra-cavity lens. The cavity mode has two waists which are located at the output coupler and the center of the gain cell. The gain cell is made with ConFlat® components which support high vacuum, and the windows are anti-reflection coated on both sides to minimize roundtrip loss. The gain cell is connected to an oven containing an ampoule of naturally-occurring Rubidium. A cylinder containing research-grade ethane gas is also connected to the gain cell, and the ethane pressure is controlled with a regulator. The oven and gain cell are each wrapped with heating wire. The windows are wrapped with a separate heating wire which is kept at a slightly higher temperature than the rest of the cell, in order to prevent condensation of Rb vapor on the windows.

The optical pump is produced by amplifying the output of a Toptica tunable diode laser with a Sacher Lasertechnik tapered amplifier (TA). This optical pump beam is s-polarized so that it is reflected into the gain cell by a polarizing beam splitter (PBS). A PBS at the other end of the gain cell expels the portion of optical pump not absorbed by the gain atoms, so that the optical pump does not make it through the output coupler. Because of the presence of the PBS's, only p-polarized light experiences roundtrip gain. Thus, the laser output is p-polarized. The optical isolator prevents directional mode competition by ensuring lasing in only one direction, but it also rotates the input light by  $45^\circ$ . Thus, a half-wave plate is placed directly after the isolator in order to rotate the light back to p-polarization. Because the gain profile is several GHz wide, while the cavity free spectral range is approximately 400 MHz, an etalon is necessary to eliminate longitudinal mode competition and mode hopping. Additionally, rotation of the etalon provides tunability of roundtrip optical path length and therefore detuning of the DPAL output frequency.

A fraction of the DPAL output goes to a photodetector, while the remainder is diverted to an acousto-optic modulator (AOM). The frequency of the modulating acoustic signal is approximately 1.518 GHz (half the ground-state hyperfine splitting in  $^{85}\text{Rb}$ ) and is produced by a voltage-controlled oscillator (VCO). The sidebands are separated spatially, and the first-order upshifted sideband is reflected back into the AOM to produce a double-shifted beam, which is then diverted with a beam splitter. This upshifted Raman probe beam has a maximum power of a few hundred microwatts, which is not strong enough to provide the range of Raman depletion necessary for comprehensive characterization thereof. Thus, the Raman probe is amplified through another TA. In addition to the amplified beam, the TA produces some stimulated emission with a spectrum hundreds of GHz wide. The holographic grating separates all unwanted frequency components from the TA output so that the Raman probe beam is spectrally pure. This Raman probe is then injected into the Raman cell with a PBS. In order to suppress sensitivity to Doppler broadening, it is necessary for the Raman probe to propagate in the same direction as the intra-cavity lasing beam for maximum two-photon interaction.

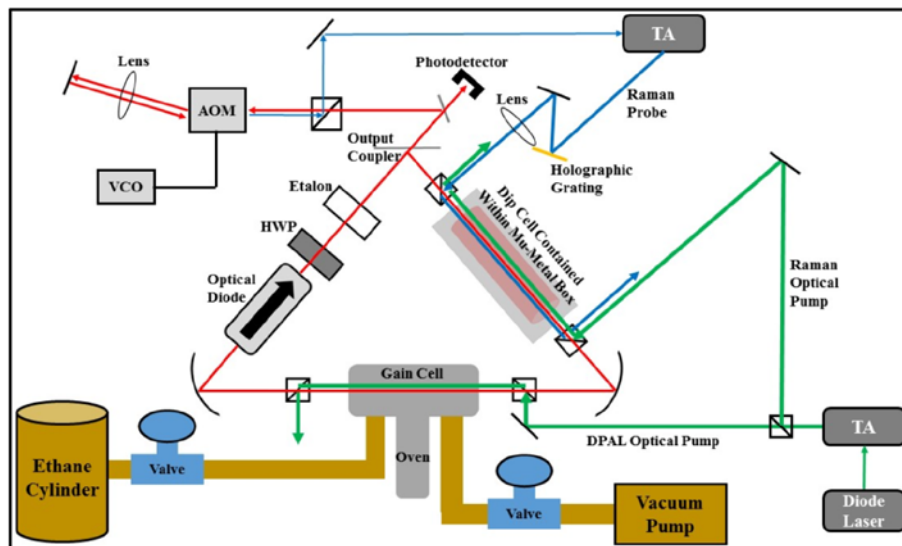


Fig. 6. Schematic of the experimental setup for realizing a superluminal laser. See text for details.

The Raman chamber is a sealed quartz cell containing pure  $^{85}\text{Rb}$  vapor. In order to prevent Zeeman splitting, heating wire is wrapped around the cell bifilarly, and the cell is housed inside a mu-metal box. A fraction of the optical pump (the same one as used in the gain cell)

is used as the optical pump for the Raman cell. The direction of propagation of the optical pump beam does not matter since it provides one-photon excitation. As such, injecting the optical pump in the counter-propagating direction circumvents the need to combine the Raman probe and the optical pump with a beam splitter, which would waste half of the power and require more optical components.

Theoretically the Raman interaction should be maximized when the frequency difference between the Raman pump and the Raman probe,  $\Delta$ , is equal to  $\omega_{21}$ , the  $^{85}\text{Rb}$  ground-state hyperfine splitting. In this experiment,  $\delta_{AOM}$  (which equals  $\Delta - \omega_{21}$ ) is scanned about a central value of zero [Fig. 5(b)]. The photodetector [Fig. 6] monitors the laser output power versus  $\delta_{AOM}$ . This measurement is made for several different values of Raman probe power.

In this experiment, the gain cell and the dip cell are each 10 centimeters in length. The gain cell is heated to a temperature of 120°C and contains ethane with pressure of 0.06 atm, while the dip cell is at a temperature of 100°C. The DPAL optical pump is 200  $\mu\text{m}$  in radius and 1.2 W in power, while the Raman optical pump is 1000  $\mu\text{m}$  in radius and 10 mW in power.

### 5.2 Experimental results and comparison to numerical simulations

Figure 7 shows the DPAL output power vs. the pump-probe detuning for six different values of Raman probe power. Figure 7(a) shows the experimentally observed signals, while Fig. 7(b) shows the corresponding numerical results. In each case, the horizontal axis is  $\delta_{AOM}$  while the vertical axis is the output power of the DPAL.

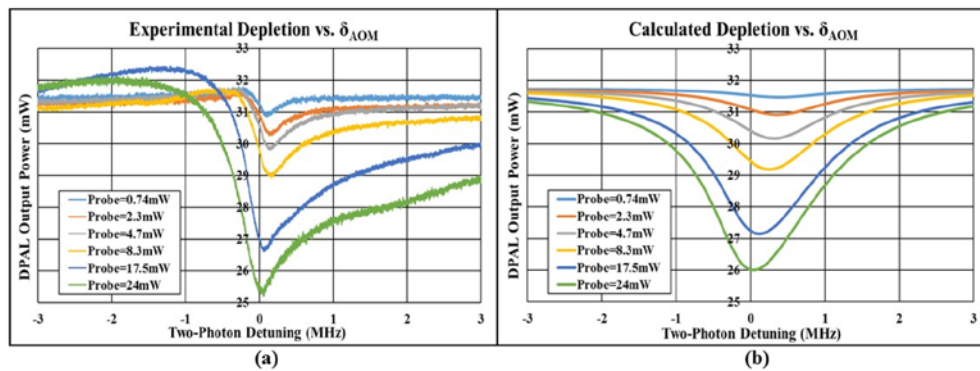


Fig. 7. (a) Experimentally observed Raman depletion; (b) numerically-calculated Raman depletion vs.  $\delta_{AOM}$ .

There appears to be reasonable qualitative and quantitative agreement between the numerical model and the experimental data. The depth and width of depletion both increase monotonically with increasing Raman probe power, with values matching reasonably well between theory and experiment. However, there are two main discrepancies to note: First, the experimental data appears to have a higher degree of asymmetry than the numerical model, especially for higher Raman probe power. Second, the calculation shows the dip shifting towards the left with increasing Raman probe power, whereas the dip location is roughly constant in the experimental data.

There are a few potential sources of these discrepancies. First, our model for the atomic transitions is somewhat simplified, both for the DPAL gain and Raman depletion. Specifically, states  $|1\rangle$ ,  $|2\rangle$ ,  $|3\rangle$  and  $|4\rangle$  each contain several Zeeman sub-levels, but are treated as a single state. Since the DPAL gain is quite broad, ignoring these details is not likely to affect the numerically-calculated DPAL gain spectrum significantly. Furthermore, for the data shown in Fig. 7(a), the parameters affecting DPAL gain are held at constant

values. Thus, simplification in the modeling of the DPAL gain is unlikely the source of the discrepancy. In contrast, the Raman depletion process has a much narrower bandwidth, and the details of the energy levels mentioned above may affect the spectral shapes of the dip. In the Raman cell, only the  $^{85}\text{Rb}$  isotope is relevant, and the details of state  $|4\rangle$  can be left out since it is used only for optical pumping. Taking into account the details of states  $|1\rangle$ ,  $|2\rangle$  and  $|3\rangle$  would require us to consider a total of 24 Zeeman sublevels. The matrix that determines the evolution of the system (based on the density matrix approach) has a size of  $N^2 \times N^2$ , where  $N$  is the number of energy levels. Thus, accounting for every Zeeman sublevel would increase the size of this matrix by a factor of  $(24/3)^4 = 4096$ . Given that our algorithm for solving the laser power and frequency is iterative, such an increase would enormously inflate the computation time, thus making it very difficult to explore the parameter space.

It is also important to note that in the numerical model for the Raman depletion, we have assumed that the Raman pump couples only to the  $|2\rangle$ - $|3\rangle$  transition, and not to the  $|1\rangle$ - $|3\rangle$  transition, while the Raman probe couples only to the  $|1\rangle$ - $|3\rangle$  transition, and not the  $|2\rangle$ - $|3\rangle$  transition. In reality, for the Raman pump and Raman probe, there is coupling to both of these transitions, and the difference between the degree of coupling to the  $|1\rangle$ - $|3\rangle$  transition and the  $|2\rangle$ - $|3\rangle$  transition depends on the detuning with respect to state  $|3\rangle$ . However, developing codes that go beyond this approximation is difficult, because it is no longer possible to make the rotating wave approximation, and one must take into account higher order harmonics of the beat note between the Raman pump and the Raman probe [22]. This approximation may account for the absence of asymmetry in the theoretical results. In the near future, we will develop a more comprehensive code that will not make these approximations and use it to determine whether the discrepancies between experiment and theory can be eliminated.

Figure 8(a) shows the theoretical change in the laser frequency versus changes in roundtrip cavity length, while Fig. 8(b) shows the corresponding enhancement factors. The enhancement factor can be thought of as the factor by which the slope of  $\Delta f / \Delta L$  in Fig. 8(a) is increased relative to the slope of the dotted line. As expected, the effects which create superluminal enhancement become more pronounced with increasing values of Raman probe power. For example, a Raman probe power of 24 mW yields an enhancement factor as high as 190 ( $= 10^{2.28}$ ), as shown in Fig. 8(b). In principle, the enhancement factor can be several orders of magnitude greater than unity with the proper choice of experimental parameters. The frequency range of this enhancement is limited by higher-order nonlinear terms in the effective dispersion profile of the lasing beam. As mentioned previously, we are currently working on achieving high enough stability in the experiment so that we can directly measure this enhancement factor.

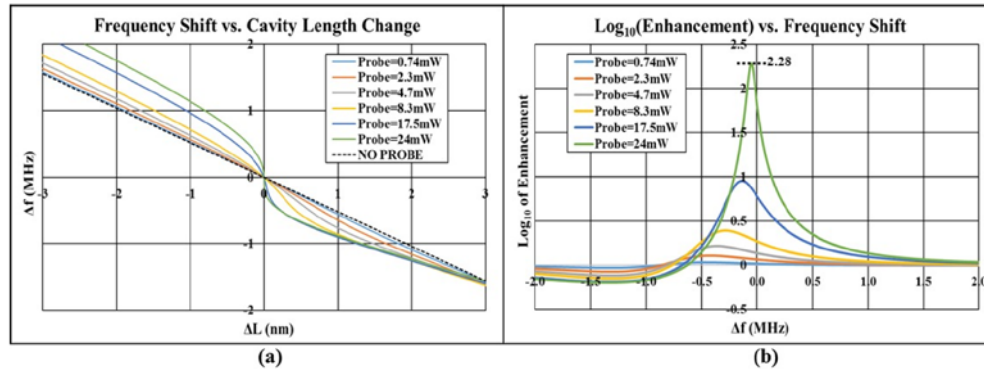


Fig. 8. (a) Frequency shift versus cavity length change for various values of Raman probe power. The dotted line represents change in DPAL output frequency vs. cavity length change for a conventional laser without Raman depletion; (b): Sensitivity enhancement factors (log scale), calculated as the ratio of the slope of  $\Delta f / \Delta L$  with Raman depletion to the slope of  $\Delta f / \Delta L$  without Raman depletion (dotted line in Fig. 8(a)).

## 6. Summary and future work

We have demonstrated a laser with a narrowband dip within a broader gain profile, the behavior of which matches reasonably well with our computational density matrix model. With the proper choice of parameters, such a laser can be several orders of magnitude more sensitive to perturbations in cavity length than a conventional laser interferometer. Therefore, such a device has the potential to advance the field of high-precision metrology, with applications such as vibrometry, accelerometry and rotation sensing.

Among our immediate goals are improving the quality and stability of our measurement systems so that we can directly measure superluminal effects. We are also investigating alternative schemes for realizing superluminal enhancement. Comparison of our theoretical model with experimental results indicates that the observed dip for one set of parameters corresponds to a superluminal laser with an enhancement factor of  $\sim 190$ , and much higher values of this factor can be realized with further tuning of parameters.

## Funding

AFOSR grant #FA9550-10-01-0228, AFRL contract numbers FA8651-13-C-0011 and FA8651-13-C-0018, and NASA contract numbers NNM13AA60C and NNX16CM03C.